Applied Acoustics 214 (2023) 109682

Contents lists available at ScienceDirect

Applied Acoustics

journal homepage: www.elsevier.com/locate/apacoust

An experimental investigation on the effect of in-flow distortions of propeller noise

Federico Petricelli [a,c], Paruchuri Chaitanya [a,*], Sergi Palleja-Cabre [a], Stefano Meloni [b], Phillip F. Joseph [a], Amin Karimian [a], Suresh Palani [a], Roberto Camussi [c]

[a] Institute of Sound and Vibration Research, University of Southampton, Southampton, SO17 1BJ, UK
[b] University of Tuscia, Viterbo, 01100, Italy
[c] University of Roma Tre, Rome, 00146, Italy

ARTICLE INFO

Keywords:
Propeller noise
Interaction tones
Tonal noise
Broadband noise

ABSTRACT

Propellers usually operate in non-uniform flow conditions, leading to significant levels of noise generation due to interaction with the leading edges of the propeller blades. Under these flow conditions, the noise generated can be substantially different from the rotor-alone self-noise generated under uniform mean flow conditions. This paper presents an experimental investigation aimed at studying the far-field noise due to a two-bladed propeller immersed in a controlled non-uniform flow with known characteristics. This paper presents the results of a parametric study with different degrees of flow non-uniformity generated from different geometric obstructions located in the jet nozzle, while maintaining constant thrust. Measurements of the radiated noise show that the incoming mean flow non-uniformities under investigation in this study cause a significant increase in tonal amplitudes of the blade passing frequencies of harmonic orders greater than 2. At the first two blade passing frequencies the tones are dominated by the rotor-alone 'Gutin-type' tones resulting from the steady blade loading. The measured noise spectra are compared with predictions from a simple frequency-domain flat plate model. The analytical model will be shown to capture the main features of the interaction tonal noise spectrum and directivity.

1. Introduction

Global attention around small Unmanned aerial vehicles (UAVs) and Urban Air Mobility (UAM) aircraft has grown exponentially in recent years. This interest is mainly due to the capabilities of such aircraft and their wide range of possible uses. Their versatility allows them to be used in both military and commercial settings. The ability to perform dangerous or expensive tasks more cheaply than manned vehicles has marked a rapid increase in their use. Some Federal Aviation Administration (FAA) projections identify a substantial projected growth in the number of commercial UAVs up to 2039 [1]. The most active sector currently is the drone delivery market. Some e-commerce giants have already obtained approval from the FAA for package delivery. According to estimates by MarketsandMarkets [2], the drone delivery market will reach a value of 39 billion in 2027. However, one of the main obstacles to further market growth is the public acceptance of these aircraft due to their emitted noise [3].

1.1. Early propeller noise research

A review of the early research into propeller noise was presented by Morfey et al. [4], who provided an overview of the main mechanisms of aerodynamic sound generation. Propeller noise may be classified into the tonal noise due to the steady blade loading noise, thickness and mean wake interactions, and the broadband noise mainly due to the turbulence interacting with the blades and trailing edge boundary layer turbulence. A survey of the main propeller noise sources is presented by Hubbard et al. [5] and Marte et al. [6]. Thickness noise is associated with the volume displacement of the propeller blade, while loading noise is due to the steady pressure distribution over the blade itself, which appears unsteady in the stationary reference frame. Thickness noise can be interpreted as a monopolar source, loading noise as a dipolar source and broadband noise as dipolar and quadrupolar source, as formally identified in the Ffowcs Williams and Hawkings' analogy [7].

* Corresponding author.
E-mail address: c.c.paruchuri@soton.ac.uk (P. Chaitanya).

https://doi.org/10.1016/j.apacoust.2023.109682
Received 5 May 2023; Received in revised form 16 September 2023; Accepted 2 October 2023
Available online 20 October 2023

1.2. Propeller noise due to in-flow distortions

Propellers generally operate in non-uniform mean and turbulent flows as described by, for example, Xie et al. [8]. Non-uniformity and distortions in the incoming flow can be due to many factors, including the interaction of the flow with the wing and a pylon used to support the propeller, as pointed out by Meloni et al. [9]. Subramanian et al. [10,11] employed non-uniform flow generators to investigate the free-field directivity of a propeller immersed in three and four-cycle azimuthal flow fields. So-called installation effects are widely studied and numerous experimental campaigns have been carried out to better understand their effects on radiated noise. Roger et al. [12] studied the tonal noise coming from a propeller in the near-wake of a wing, while, in the future perspective of distributed electric propulsion on UAVs, Acevedo et al. [13] experimentally characterised the acoustics of a pair of side-by-side corotating subsonic propellers mounted near a wing trailing edge. In the same framework, Paruchuri et al. [14] investigated the mechanisms of propeller-wing interaction noise, showing a significant increase in tonal and broadband noise in case of increased wing-tip vortex flow interaction. Enhanced noise generation in the presence of propeller-wing interaction is also observed in the investigations by Borchers et al. [15] and Jamaluddin et al. [16]. Di Marco et al. [17] investigated a pusher propeller configuration installed on a wing. Again, the dominant noise generation mechanism was found to be due to the propeller-wing interaction (also confirmed through beamforming). Another source of flow non-uniformity is due to atmospheric turbulence caused by wind and thermal effects, as described by Hanson et al. [18]. This type of unsteady in-flow distortion is related to the elongation of turbulent vortices as they approach the propeller. The suction effect upstream of the propeller results in the presence of a strong streamtube contraction, which stretches the eddies and significantly increases the streamwise length-scale while reducing the transverse length-scale.

In a theoretical study Majumdar et al. [19] presented an analysis of propeller in-flow distortion noise and provided a framework for understanding how larger eddy length-scales result in higher tonal peaks, while smaller eddies contribute to higher broadband content. Spectrally broadened (hay-stacked) tones at the blade passing frequencies are generated when highly stretched vortices are periodically “cut” by the propeller blade. An experimental verification of this phenomenon is presented by Gojon et al. [20] who measured the far-field noise due to a propeller interacting with a beam, revealing a high amplification of the tonal interaction amplitudes. A similar experiment was performed by Yauwenas et al. [21], who found similar results. They also investigated the effect on noise due to a grid located upstream of the propeller. The noise due to distortions in the incoming flow approaching the propeller was compared to the noise in a completely uniform flow. In the same framework, Wojno et al. [22,23] experimentally characterised the rotor noise in response to grid-generated turbulence. Jamaluddin et al. [24] also conducted a testing campaign to investigate the effect of turbulence ingestion on propeller noise, showing that strong axial and radial velocity fluctuations can significantly alter the radiated acoustic pressure. In particular, these additional sources then result in noise defined by a broadband contribution, related to the small-scale random turbulence in the flow, and a tonal contribution, related to the interaction of the mean in-flow distortions with the blade leading edges. Tonal noise was found to be much higher in Sound Pressure Level (SPL) than the relative broadband noise. In this regard, many experiments have been carried out to better understand the mechanisms and possible implications of noise generation [25–28]. Understanding the relationship between the characteristics of the mean flow distortions and the subsequent noise generation is therefore essential to enable the design of low noise propeller configurations. That is to ensure that the installation of the propeller does not lead to high levels and type of mean in-flow distortions does not lead to unacceptably high levels of tonal interaction noise.

1.3. Theoretical studies of propeller noise

A number of time and frequency domain formulations have been developed for the prediction of tonal noise due to propellers. The advantage of a formulation in the frequency domain is that it avoids the calculation of retarded blade positions, unlike a time domain formulation. One of the earliest theories of propeller noise is due to Gutin in 1948 [29,30], for steady loading noise. This model was later generalised by Goldstein [31] to include non-uniform inflow. A comprehensive theoretical study on helicopter radiated noise was carried out by Lowson et al. [32], who derived an exact solution for far-field and near-field noise radiation. In 1971, Wright et al. [33] described a theory for the prediction of tonal noise from rotating periodic sources (rotors). More recently, Zhou et al. [34] proposed a frequency domain formulation for the prediction of propeller tonal and broadband radiation. Carley et al. [35] later proposed an exact and general method for the evaluation of the acoustic field of a rotating source in a non-uniform potential flow. Similarly, Glegg et al. [36] described a time-domain method for predicting broadband in-flow distortions noise starting from turbulent velocity correlation measurements upstream of the propeller.

1.4. Scope and novelty of the current paper

Despite the previous work in propeller noise due to in-flow distortion, a comprehensive description of the problem based on systematically imposing the in-flow characteristics has not been fully addressed. For this reason, an attempt is made in this paper to provide for the first time an exhaustive and detailed insight into the actual sound sources under such flow conditions and their implications on radiated noise.

In the present discussion, such non-uniformities are generated experimentally by using aluminium plates of different shapes placed right at the outlet of the wind tunnel nozzle, in order to obtain different azimuthal jet distortions. Such distortions have been chosen as they can be representative of real applications, close to new experimental UAMs and UAVs concepts. Furthermore, this allows us to well control the velocity harmonics, which will be seen to be fundamental for the comparison with the prediction model. Great attention is paid to these distortions and what they determine both in terms of tonal noise, with interaction tones, and in terms of broadband noise. In particular, the velocity spectrum is also analysed in detail to investigate the real sources of broadband noise content and how they change in non-uniform flows, showing that broadband noise is relatively unaffected compared with the tonal amplitudes. Furthermore, the experimental data are compared with a frequency domain formulation, proposed by Xie et al. [8], to predict the far-field tonal noise produced by propellers operating in non-uniform flows, showing that a simple analytic model based on flat plate theory is capable of capturing the changes in radiated noise due to differences in the mean flow distortion. The mathematical model is based on the use of the free-field Green’s function, coming from the solution of the acoustic analogy. A numerical method was used for the implementation of the analytical model. This is used to demonstrate that low order blade passing frequencies ($n = 1, 2$) are relatively unaffected by inflow distortion since these are dominated by rotor alone (Gutin-type) tones due to mean blade loading. On the other hand, the higher blade passing frequencies ($n > 3$) are most sensitive to the details of the mean in-flow distortion since these are most affected by the higher order velocity harmonics, which of course are most affected by small differences in the flow distortion.

The work is organized as follows. The experimental set up is shown in Section 2 while the flow characterisation is presented in Section 3. In Section 4, far-field noise characteristics are reported for both tonal and broadband noise. Section 5 mentions the theory behind the mathematical formulation and compares analytical predictions to experimental results. Conclusions are reported in Section 6.

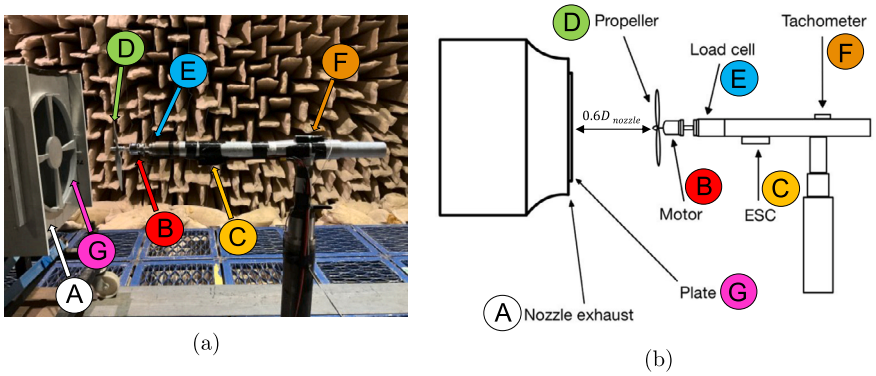

Fig. 1. General Set up of the propeller rig: (a) Lateral view; (b) Schematic view.

2. Experimental set up

This section describes the experimental set up used to investigate the relationship between mean in-flow distortions and the resulting noise generation. The experimental campaign was conducted in the anechoic wind tunnel facility at the Institute of Sound and Vibration Research at the University of Southampton. The chamber has dimensions of $8m \times 8m \times 8m$ with a cut-off frequency of $80Hz$ [37].

A twin-bladed APC Sport Model propeller ($12 \times 5.5''$, where 12 and 5.5 are the propeller diameter and pitch in inches, respectively) was situated in the open jet of the wind tunnel with various obstructions introduced in the jet nozzle to vary the character and intensity of the in-flow distortion. The dominant basis for the primary propeller airfoil shape is similar to the NACA 4412 and Clark-Y airfoils. The propeller was positioned on the jet axis at a distance of $0.6D_{nozzle}$ ($20cm$) from the nozzle outlet (Fig. 1), in order to avoid acoustic scattering effects from the nozzle itself. The rectangular nozzle has dimensions of $35cm \times 50cm$. An aluminium plate with a circular aperture with radius of $17.5cm$ was attached to the nozzle outlet in order to obtain a uniform circular jet. This experimental configuration was taken as the baseline configuration against which the noise due to azimuthal in-flow distortions could be compared.

2.1. Motor, load cell and data acquisition systems

The propeller was powered by TURNIGY AERODRIVE SK3 - 3542-800KV Brushless outrunner motor and controlled using a Master Mezon 135 opto electronic speed controller unit. The motor was mounted on MINI45 ATI 6-axis loadcell, which allowed the measurement of the forces and torques in all three orthogonal directions aligned with the propeller axis. The propeller rig arrangement and its schematic view are shown in Fig. 1a and Fig. 1b, respectively.

The precise rotational speed of the propeller was measured by using an ICP Laser Tachometer sensor and reflective tachometer tape. Sensor data collection was fully automated using National Instrument's Labview modules. A CompactRIO system with a real-time module was used to control the required thrust and keep it constant at the desired speed. Details of the functioning of the latter module can be found in the thesis by Fanghzi [38].

2.2. Microphone array and flow non-uniformities

Far-field acoustic measurements were performed by using 15 half-inch free-field microphones (B&K type 4189), with a frequency range between $6.3Hz$ and $20kHz$. A G.R.A.S. Sound Calibrator 42AB was used for the calibration, with an output level of 114 dB at a reference frequency of $1kHz$. The microphones were distributed over a circular arc, whose centre was positioned at $6.5D_{prop}$ ($2m$) from the centre of the propeller, between the angles 45° and 115° (at 5° intervals) from the flow direction, as shown in Fig. 2a. For clarity, a schematic view of the microphone array is also shown in Fig. 2b. Noise measurements were acquired for $10s$ at a sampling frequency of $40kHz$, in order to capture the characteristic time of the phenomenon ($\frac{1}{BPF} \sim 0.005s$). In addition, noise spectra were calculated using a Hanning window size of 8192 data points.

Flow non-uniformities were generated using aluminium obstructions within the baseline configuration (Full Circle layout) at the nozzle discharge. In order to study the effect on noise due to change of azimuthal non-uniformities in the incoming flow, different obstruction geometries were investigated, referred to as: Cross, Half cross and 180° (or Half circle) configuration, as shown in Fig. 3. These flow obstructions were

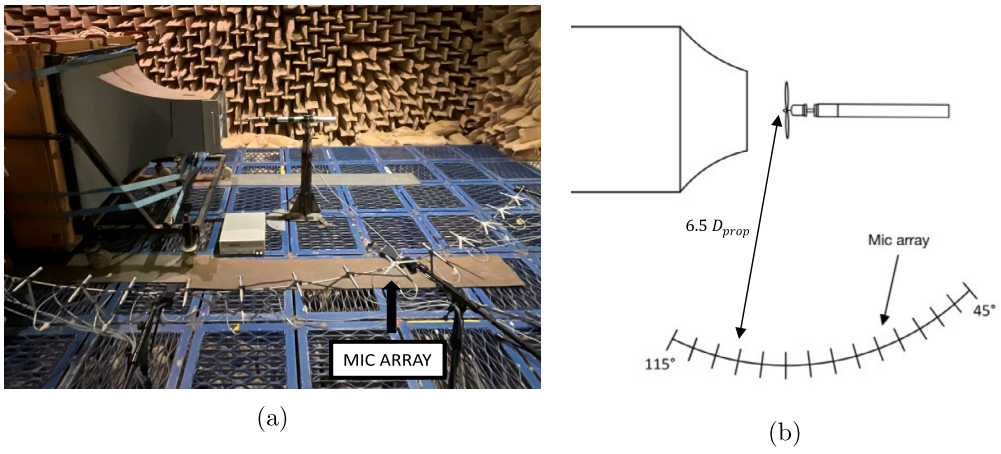

Fig. 2. Microphone array: (a) Top view; (b) Schematic top view.

T [N]	U [m/s]	Baseline	Cross	Half Cross	Half Circle
10	0				
	10				
	20				

Fig. 3. Test matrix.

designed to ensure that at least one azimuthal velocity harmonic was present around the jet circumference. In the Cross and Half cross configurations, the radial obstructions were 10° in width and the central hub had a radius of $5cm$. Due to the different level of flow blockage produced by each obstruction, the wind tunnel fan speed was adjusted to deliver the same desired jet velocity at the nozzle outlet.

2.3. Configurations tested

The propeller in the distorted in-flow was operated at a constant thrust value $T = 10N$. Noise measurements for each flow obstruction were repeated at the different incoming jet velocities of $U = 0, 10, 20\ m/s$. A summary of the tests performed is shown in the Test Matrix in Fig. 3.

3. Flow characterisation

Measurements of the mean and unsteady in-flow at the nozzle exhaust were carried out using a single hot wire anemometer (TSI IFA-300 CTA), with the objective of quantifying the degree of flow non-uniformity. A 3 Axis Traverse System T3D was used to move the hot wire, which was positioned at $0.4\ D_{nozzle}$ from the nozzle exhaust to characterize the flow impinging onto the propeller. The hot wire signals from all nozzle configurations have been analyzed, with the exception of the Half cross configuration, as it is nearly identical to the flow profile of the Cross configuration in the upper and low sections. The different hot wire sweeps are indicated in red in Fig. 4.

The variation in velocity was measured along the radial direction of the jet, as shown in Fig. 4a, 4b and 4d. As for the Half Circle configuration, the velocity was also acquired along two 135° arcs at 60% and 80% of the jet radius, as shown in Fig. 4e. For the Cross configuration, hot wire measurements were made over a 90° circular sector, as shown in Fig. 4c. The number of points acquired was varied for each configuration, to concentrate the measurement points in their respective shear layer regions. For the sake of brevity, the flow characterisation is reported only for the Full Circle and Cross configurations with a jet velocity $U = 20\ m/s$, which has been consistently measured for each test case by using a Pitot tube, in order to have the same desired flow velocity at the nozzle outlet for all the configurations.

3.1. Mean flow

The mean velocity profiles along the jet radius for the Full circle and Cross configurations are shown in Fig. 5a and 5b, respectively.

The nozzle shear layer can be clearly seen in both configuration, extending from 70% to 100% of the nozzle radius. Furthermore, for the Cross configuration, a second shear layer is observed near the centre of the jet due to the central circular hub (see Fig. 3). A more complete visualisation of the mean flow profile due to the different obstruction geometries in the flow is reported in Fig. 6, which shows the mean velocity field map for the circular sector of the Cross configuration.

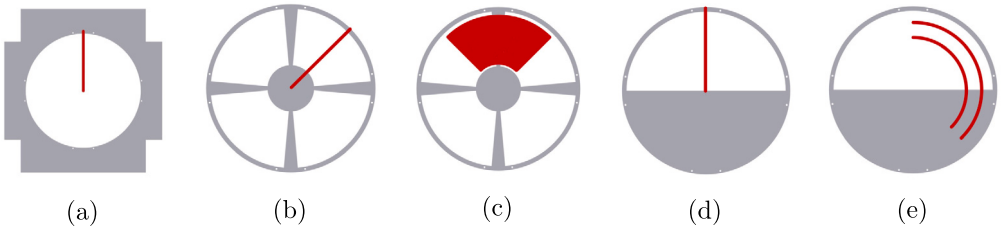

Fig. 4. Hot wire sweeps: (a) Full circle radius; (b) Cross radius; (c) Cross sector; (d) 180° radius; (e) 180° arcs.

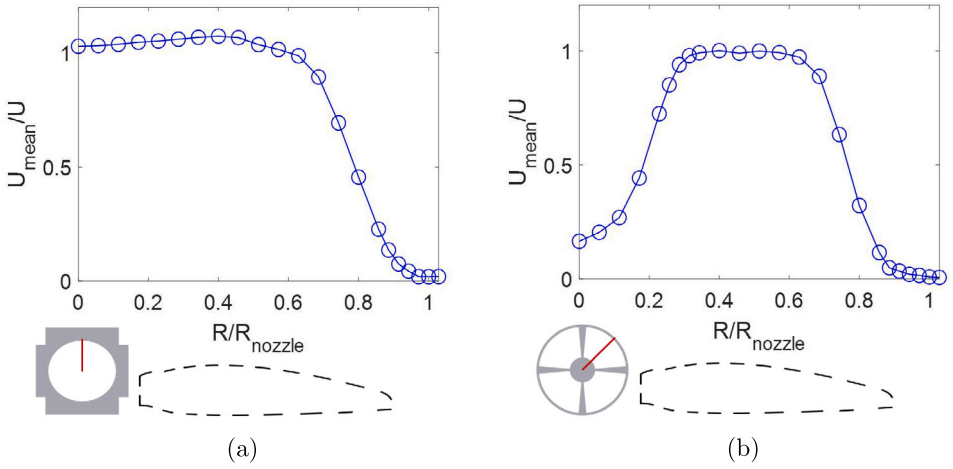

Fig. 5. Mean velocity profiles on the radial direction of the jet: (a) Full circle configuration, (b) Cross configuration. The dashed outline of the blade is also reported to highlight the propeller position.

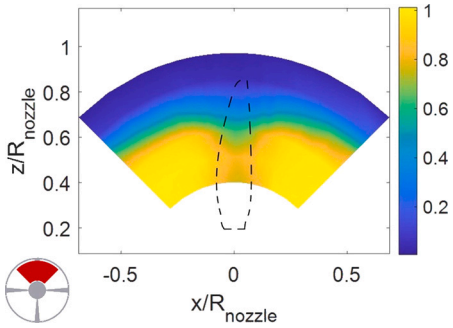

Fig. 6. Mean velocity field for a circular sector of the Cross configuration. The dashed outline of the blade is also reported to highlight the propeller position.

Note that here the effect of the shear layer development provides a decrease of the average velocity behind the cross-segment at $x = 0$ and along the z direction.

3.2. Turbulence intensity

Fig. 7a and 7b show the turbulence intensity profiles along the jet radius for the baseline and Cross configurations, respectively.

The shear layer regions of high turbulence intensity are clearly observed. Fig. 8 shows the variation in turbulence intensity over a sector of the Cross configuration, indicated by the red region at the bottom of the figure. The flow is observed to be more turbulent at $x = 0$ and along the z direction behind the cross-segment, where wake turbulence is generated. In addition, more intense fluctuations are also observed in the area of the circular shear layer, confirming previous observations along the radial direction.

3.3. Flow spectra

This section presents the radial variation in the turbulence velocity frequency spectrum, which we show in Section 4 has a direct relationship to the noise radiated by aerofoils rotating through the flow distortion. The Power Spectral Density of the velocity along the nozzle radius for the Full Circle and Cross configurations is shown in Fig. 9a and 9b. The velocity spectral contours clearly indicate regions of higher turbulence intensity in the shear layers generated by the hub and by the outer edge. Furthermore, some tonal peaks can be seen in the mid-frequency range, even in the absence of obstructions. These peaks are found precisely at the blade passage frequencies, and are due to the air displacement of the blade, as the hot wire was very close ahead of the propeller during the velocity measurements.

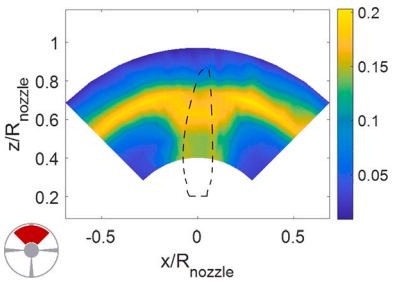

Fig. 8. Turbulence intensity field for a circular sector of the Cross configuration. The dashed outline of the blade is also reported to highlight the propeller position.

The velocity spectra at the two representative radial positions of 84% and 28% of the nozzle radius are shown in Fig. 10a and 10b, respectively. Note that a completely different velocity spectrum is obtained near the hub in the Full circle configuration, where the jet potential core is dominant. In particular, Fig. 10a and 10b show the indication of the gradient in red, which is similar in the shear layers areas with a decay rate of f^{-2}, suggesting very similar turbulence characteristics in both regions.

4. Far-field noise characteristics

In this section we present the noise spectra for a microphone positioned at 90° to the flow direction, i.e. in the plane of the propeller. The noise data at the inflow speed of $U = 10\,m/s$ is not reported here, since it shows similar qualitative behaviour to the results reported here for $U = 20\,m/s$. In the following discussion we treat the behaviour of the tonal and broadband noise separately.

4.1. Tonal noise

Tonal noise can be seen as determined by loading tones, due to the pressure distribution on the propeller blade, and interaction tones, due to blade interaction with wakes, distortions in the flow and recirculation. It will be explained below in section 5 that the first $2-3$ tones are mainly due to loading noise, as Gutin's formulation [29] predicts a very clear decay trend and levels in agreement with experimental data. The higher order tones are therefore interaction tones, as loading tones becomes increasingly lower in amplitude at higher harmonics.

The comparison of the noise spectra, in the hover condition ($U = 0\,m/s$), between the Full Circle, Cross, Half cross and 180° configura-

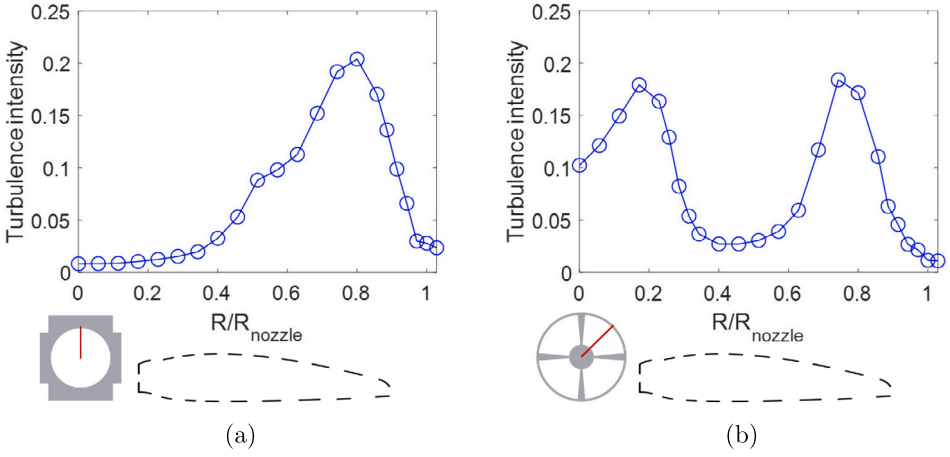

Fig. 7. Turbulence intensity on the radial direction of the jet: (a) Full circle configuration, (b) Cross configuration. The dashed outline of the blade is also reported to highlight the propeller position.

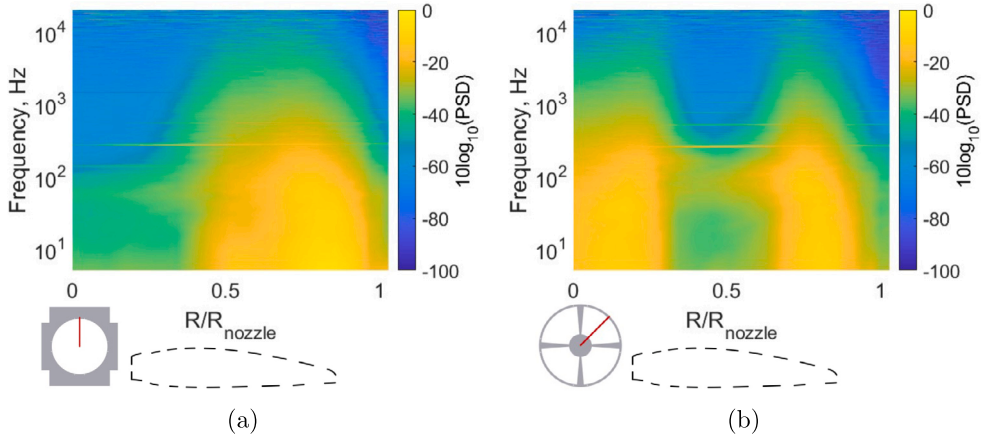

Fig. 9. Power spectral density of the flow velocity: (a) Full circle configuration, (b) Cross configuration. The dashed outline of the blade is also reported to highlight the propeller position.

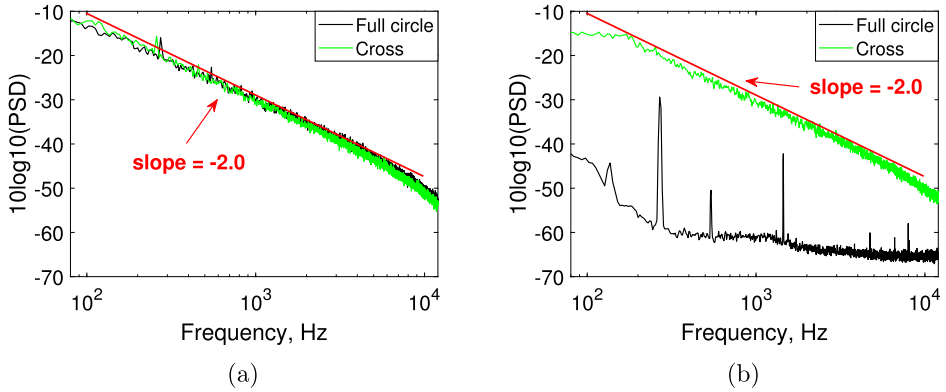

Fig. 10. Power spectral density of the flow velocity for Full circle and Cross configurations: (a) at $R/R_{nozzle} = 0.84$, (b) at $R/R_{nozzle} = 0.28$.

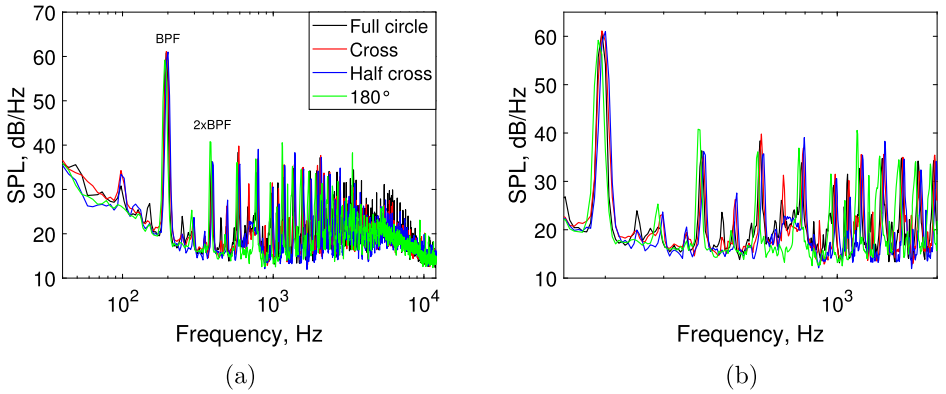

Fig. 11. Propeller noise spectra at $U = 0\,m/s$: (a) Comparison between Full circle, Cross, Half cross and 180° configurations; (b) A zoom of Fig. 11a.

tions is shown in Fig. 11a along with the BPF indication. A zoom of the most dominant peaks between $100Hz$ and $2kHz$ is shown in Fig. 11b.

Whilst in this case there is no flow from the nozzle, there remains some residual flow non-uniformity onto the propeller since it draws some low speed flow through the nozzle and the various obstructions. However, this induced velocity is not high enough to generate significant non-uniformities and, for this reason, there are no appreciable changes in the tonal peaks between different configurations.

The comparison of the noise spectra, with flow velocity $U = 20\,m/s$, between the Full Circle, Cross, Half cross and 180° configurations is shown in Fig. 12a along with the BPF indication. A zoom of the most dominant peaks is shown in Fig. 12b.

The introduction of a distorted flow onto the propeller results in pronounced non-uniformities at the nozzle outlet and, therefore, differences between the various configurations in terms of radiated noise. The interaction tones due to flow obstructions of the Cross, Half cross and 180° configurations can be observed to increase the noise by approximately 10 dB compared to when the incoming flow is uniform. This happens because the noise contribution coming from the steady loading of the propeller becomes increasingly smaller for the harmonics of

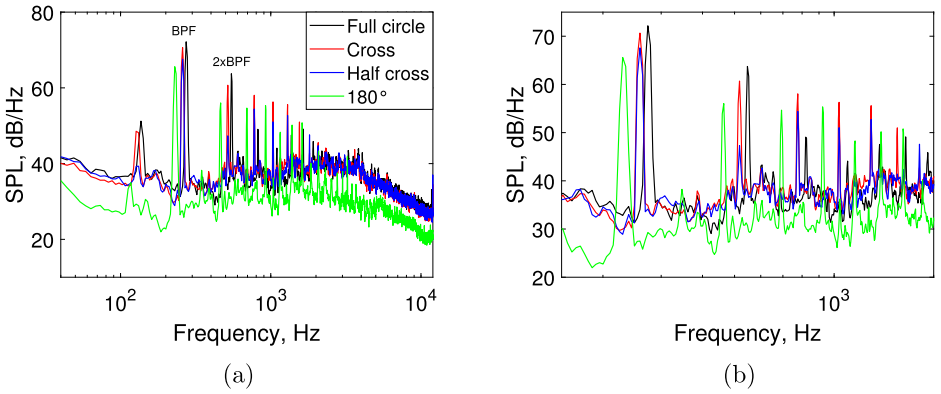

Fig. 12. Propeller noise spectra at $U = 20\,m/s$: (a) Comparison between Full circle, Cross, Half cross and 180° configurations; (b) A zoom of Fig. 12a.

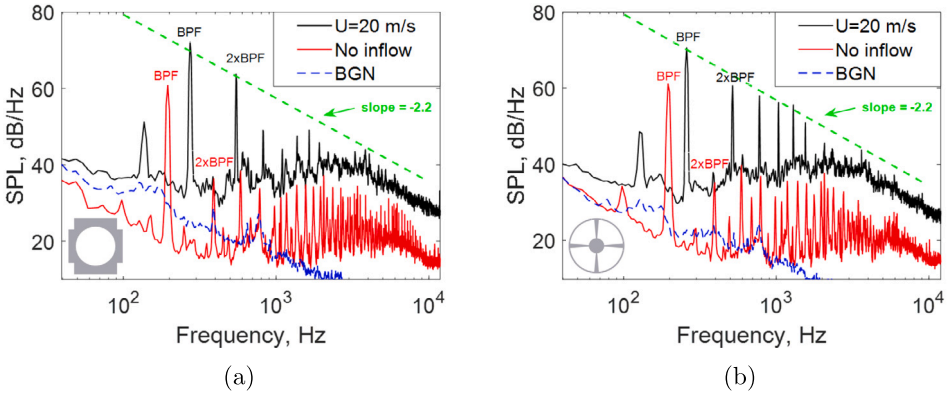

Fig. 13. Spectra comparison between propeller noise with inflow, propeller noise without inflow, background noise with $U = 20\,m/s$: (a) Full circle configuration, (b) Cross configuration.

the BPF and, at frequencies greater than the third harmonic, the contribution from interaction noise due to in-flow distortions becomes more evident.

The difference in levels for the first two BPF harmonics can be seen to be highly sensitive to the variations in the geometry of the obstructions whereby differences in tone level by as much as 7 dB can be observed, where steady loading noise would be expected to be dominant. Some of this variation may be due to variations in the torque needed to maintain the same thrust, as the propeller is required to rotate faster at the higher air mass flow rates, also resulting in a shift in the blade passing frequencies. Moreover, this frequency shift affects the sound pressure level due to the decay of the Bessel functions, which appear to be a very important term in the evaluation of the total radiated pressure (Eq. (6) in section 5). This phenomenon therefore does not occur in the hover condition (Fig. 11a). On the other hand, the broadband noise decreases significantly for the 180° configuration due to the fact that the mass flow rate is halved compared to the fully uniform case, as the nozzle outlet velocity is maintained. Thus, the turbulence interacting with the blades is reduced. Also, by considering the relative spectral widths $\Delta f/f_n$ of the spectral peaks for all types of inflow distortion, where Δf is the frequency bandwidth at 3 dB below the peak and f_n is the tonal centre frequency, no significant difference in $\Delta f/f_n$ can be seen for any cases under investigation. Thus, haystacking, caused by the large eddies generated in the shear layers, can be considered negligible in these measurements.

4.2. Broadband noise

The noise spectra for the propeller with flow is compared against the noise in the hover condition in Fig. 13a and 13b for the Full circle and Cross configurations, respectively. Also shown is the background noise spectra due to the jet without propeller present.

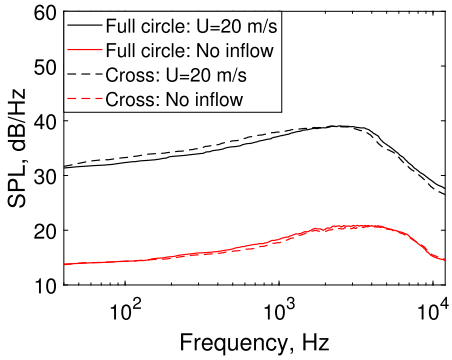

Fig. 14. Broadband noise content with and without inflow for Full circle and Cross configurations.

The interaction noise spectra shown in Fig. 13a and 13b, above about $2kHz$ can be observed to be dominated by broadband noise, whose rate of decay with frequency is approximately $f^{-2.2}$. Also, for all the nozzle configurations, there is an increase in the broadband noise content between the hover condition and the case with incoming flow. This can be observed more clearly in Fig. 14, where only the broadband content of the noise spectra seen in Fig. 13a and 13b is shown. This component has been obtained by using a "median filter", in which each frequency point in the spectra is replaced by the median value of the spectral values at 700 points either side of it.

The increase in noise with increased flow velocity is consistent with expectations, as the turbulence ($TI = 0.5\%$) in the incoming flow will

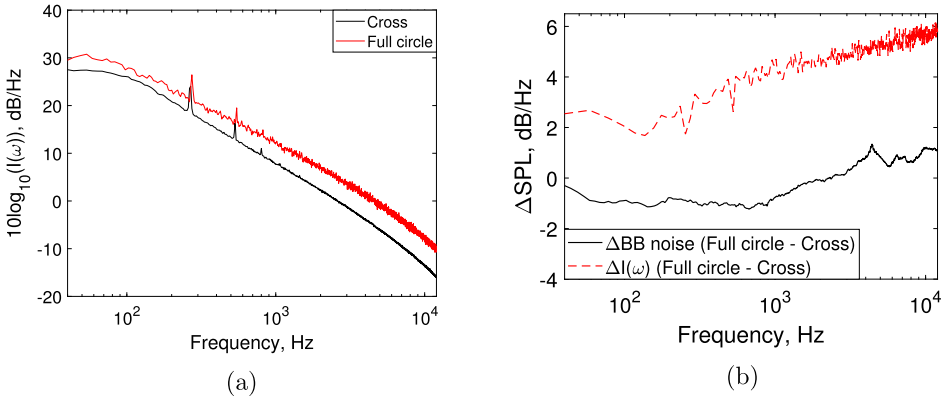

Fig. 15. (a) Velocity PSD integration over area for $20\,m/s$ inflow. (b) Broadband noise content and $I(\omega)$ differences between Full circle and Cross configurations with $U = 20\,m/s$.

interact with the propeller blade. In particular, broadband noise sources are related to the leading edge interacting with the nozzle shear layer and to the trailing edge scattering noise. Both noise sources are known to radiate with the $5-6^{th}$ power of the flow velocity. Therefore, higher levels are expected as the propeller needs to rotate faster to generate the same thrust than in the hover condition. In order to identify the cause of the difference in noise between the two obstructions, we now examine the velocity spectra plotted in Fig. 9a and 9b ($20\,m/s$ inflow case) weighted by the cube of the velocity $(\Omega r)^3$, which we shall refer to as $I(\omega)$:

$$I(\omega) = \int_S S_{uu}(\omega, r)(\Omega r)^3 r\, dr, \tag{1}$$

where the integral is performed over the area shown in Fig. 4c.
This velocity weighting is suggested by the expression due to Amiet for the noise due to flat plate interacting with turbulent flow, so that neglecting the frequency dependence of the blade response $S_{pp}(\omega) \propto I(\omega)$. In particular, it provides a measure for the leading edge noise, as the term U^3 appears in the expression for the evaluation of the far-field leading edge noise PSD.

The weighted velocity spectra $I(\omega)$ are shown in Fig. 15a for both the Full circle and the Cross configurations. Note that the two curves are not collapsed but present a difference (shown in Fig. 15b), indicating that, in addition to leading edge noise, the rotor self noise, i.e. trailing edge noise, gives a non-negligible contribution. Also, the difference in terms of far-field broadband noise between the Full circle and the Cross configurations appears to be less than 1.5 dB, as shown in Fig. 15b, which seems to be coherent with the logarithmic scale ratio of the rotational velocities of the Full circle ($RPM = 8226$) and Cross ($RPM = 7755$) configurations $50\log\left(\frac{RPM_{Fullcircle}}{RPM_{Cross}}\right)$, which is just 1.28 dB. This suggests that the most important broadband noise source is trailing edge self-noise, rather than leading edge noise, meaning that the main effect of inflow distortions on broadband noise is the additional flow blockage and relative mass-flow rate change. For this reason, in order to maintain the same thrust, the propeller RPM is reduced, thus leading to a decrease of the rotor self-noise.

5. Tonal noise predictions

In this section the measured increase in tonal noise at the harmonics of blade passing frequencies are compared against predictions obtained using the analytical formulation presented by Xie et al. [8] or Petricelli et al. [39], which are a generalisation of Gutin's theory [29]. In this theory the propeller blades are approximated as flat plates and the incoming mean flow distortion is decomposed into its velocity Fourier components. The mathematical formulation derives from the fundamental equation governing the generation of aerodynamic sound in the presence of solid boundaries, which can be reduced to

$$p(\mathbf{x}, t) = \int_{-T}^{T} \iint_{S(\tau)} \frac{\partial G}{\partial y_j} f_j\, dS(\mathbf{y}) d\tau, \tag{2}$$

where $f_j = -n_j(p - p_0) + n_k e_{jk}$ is the jth component of the force per unit area exerted by the boundaries on the air, n_j is the jth component of the unit inward normal $\mathbf{n}$ on the surface $S(\tau)$, e_{jk} is the (j,k)th component of the viscous stress tensor, p_0 is the pressure of the stationary background flow and T is a large finite time interval. G is the Green's function obtained from the solution, by acoustic analogy, of the forced wave equation in an unbounded medium. Now, the full model description is reported in [8], but the key passage in this approach is given by the definition of the axial component of the velocity disturbance $\tilde{u}(r_0, \theta_0)$, which can be expressed in Fourier series as:

$$\tilde{u}(r_0, \theta_0) = \sum_{n=1}^{\infty} A_n(r_0) e^{-in\theta_0} \tag{3}$$

Thus, the unsteady pressure distribution on one side of the blade is given by:

$$p(r_0, \theta_0; \tau) = \rho_0 U_0(r_0) \cos\gamma(r_0) \sum_{n=1}^{\infty} A_n(r_0) e^{-in\theta'_0} Sears(\bar{k}_{n,r_0}), \tag{4}$$

where $U_0(r_0)$ and $\gamma(r_0)$ are the total incoming velocity impinging on the blade and the geometric pitch angle, respectively at radius r_0, $\bar{k}_{n,r_0}$ is the nondimensional wave number of the nth velocity harmonic normalized by the semi-chord at radius r_0 and $Sears(\bar{k}_{n,r_0})$ is defined by the product of classical Sears aerodynamic transfer function $Se(\bar{k}_x)$ and the chord distribution

$$Sears(\bar{k}_x) = Se(\bar{k}_x)\sqrt{\frac{1-\bar{x}}{1+\bar{x}}}, \tag{5}$$

where $\bar{x}$ is the nondimensional chord coordinate ranging from $[-1, 1]$, respectively from the leading edge to the trailing edge, as introduced by Theodorsen's theory [40]. Note the importance of all the velocity harmonics, in the definition of the unsteady pressure distribution, representing precisely the incoming flow non-uniformities. Switching to the frequency domain and following the steps described in detail in [8], the total radiated pressure is obtained, which is given by

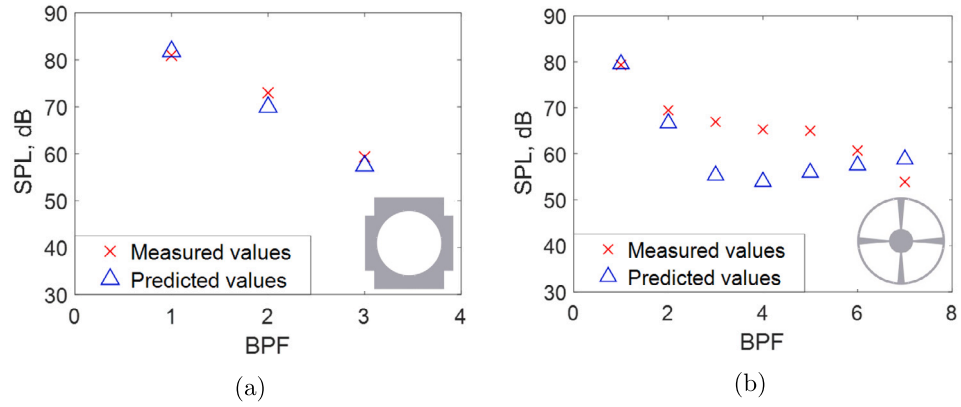

Fig. 16. Sound pressure levels comparison between measured (red crosses) and predicted values (blue triangles): (a) Full circle configuration; (b) Cross configuration.

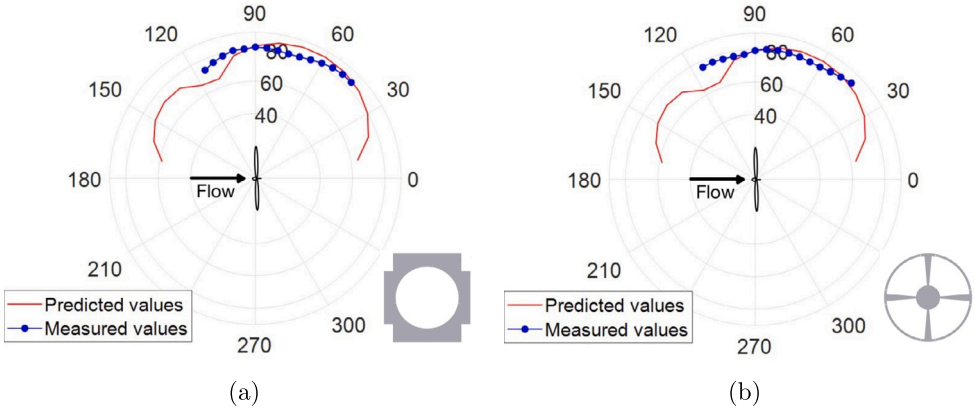

Fig. 17. Comparison of the directivity of the first BPF harmonic with inflow velocity $U = 20\,m/s$: (a) Full circle configuration; (b) Cross configuration.

$$\hat{p}(\mathbf{x},\omega) = \frac{-i\mu B\rho_0}{4\pi R_s} e^{i\mu(R_s - Mx_1)} \times \sum_{l=-\infty}^{\infty}\sum_{n=1}^{\infty} e^{i(lB-n)(\theta'-\frac{\pi}{2})}\delta(\omega + lB\Omega)\times \iint_{S_i} \left\{ n_1 \left[\frac{y_1 - x_1}{R_s} + M\right] - n_r\beta^2 \left[-\frac{r_0}{R_s} + i\sin\psi\left(\frac{lB-n}{\kappa r_0 \sin\psi} + -\frac{J_{lB-n+1}(\kappa r_0\sin\psi)}{J_{lB-n}(\kappa r_0\sin\psi)}\right)\right] - n_\theta\beta^2\frac{lB-n}{\kappa r_0}\right\} J_{lB-n}(\kappa r_0\sin\psi)\times A_n(r_0)U_0(r_0)\times\cos\gamma(r_0)e^{i\mu(M-\cos\psi)y_1}e^{-ilB\theta_0}Sears(\bar{k}_{n,r_0})\,dS(\mathbf{y}^b), \tag{6}$$

where B is the number of propeller blades, $\mu = \kappa/\beta^2$ and $\kappa = \omega/c_0$ is the acoustic wave number related to observer frequency, $\beta^2 = 1 - M^2$, M is the Mach number of the mean flow, l is the number of radiated harmonic noise order, n is the number of inflow velocity harmonic order, $\cos\psi = x_1/R_s$, $\sin\psi = r/R_s$ and $R_s = \sqrt{x_1^2 + \beta^2 r^2}$.

The comparison between measured and predicted sound pressure levels with velocity $U = 20\,m/s$ is shown in Fig. 16a and 16b for the Full circle and Cross configuration, respectively. SPLs are only reported for the first three BPF harmonics for the baseline configuration in Fig. 16a. This is because the flow is completely uniform in this situation and, consequently, there are no additional velocity harmonics to be included in the prediction model, which then only predicts loading noise. Therefore, in this case, it is not of interest to study tones of order higher than 3, as predicted levels keep decaying following the trend of the first three harmonics. A very good agreement can be observed as the measured values are very close to the predicted ones, with a maximum error of 3 dB on the second BPF harmonic. This shows that loading noise is predominant on the first 2 – 3 harmonics, while higher order harmonics are mainly due to interaction noise. In the case of the Cross configuration, in Fig. 16b, the first seven BPF harmonics are reported, so that the effect of flow non-uniformities on interaction tones can be studied. The loading noise is still captured correctly, with a minimal difference on the first two tones, while a larger error is registered from the third BPF harmonic. However, despite the large difference in SPL, the model still manages to capture a qualitative increase in the higher harmonics, which is not predicted in the case of uniform flow, and is therefore characteristic of interaction tones. Furthermore, additional causes of these differences can be caused by the assumptions of the mathematical model. The formulation does not take into account the contribution of thickness noise and makes approximations related to far-field conditions. In addition, the pressure on the blade surface is evaluated using a two-dimensional airfoil theory, which does not take into account three-dimensional effects and no recirculation and scattering are considered in the current study.

Fig. 17a and 17b show the comparison of the directivity of the first BPF harmonic with flow velocity $U = 20\,m/s$ between experimental data and analytical predictions for the Full circle and Cross configurations, respectively. Note that the local reduction around 120° on the predicted values is coherent with expectations, as Goldstein [31] also predicts the same result. A good agreement is obtained for the backward radiation in both levels and trends for Full circle and Cross nozzle exhaust configurations. The forward radiation, on the contrary, is not very well captured, as the predicted change on concavity around 120° is not present in the experimental data, probably due to the presence of small amount of noise in the acquired signal.

6. Conclusions

Experimental measurements were carried out to investigate the effects of a non-uniform flow on the far-field noise generated by a propeller. These effects were considered in terms of both tonal and broadband noise. Different nozzle layouts were considered so that different

types of non-uniformities in the incoming flow could be investigated. These non-uniformities result in the amplification of the sound pressure level of the interaction tones, which become predominant from the third harmonic BPF onwards, as the loading noise content decays. In particular, all the non-uniform flows taken into account provide an increase in the order of ten decibels, with a maximum value of 12 dB reached by using the Cross configuration. The physical explanation for this lies in the fact that the blade sees a time-varying pressure when it rotates, as it encounters a non-uniform velocity field (dictated by the nozzle geometry) and, therefore, non-stationary loads. From a mathematical point of view, the tonal peak amplification of the interaction tones is explained by the fact that other polar harmonics of the velocity are taken into account, which are representative precisely of the flow non-uniformity. The broadband noise, on the other hand, is seen to be quite unaffected by the non-uniformities taken into account, as the Full circle and Cross configurations almost have the same energy content. The most important contribution has been shown to come from trailing edge noise, i.e. rotor self-noise, which increases with propeller rotational speed. In contrast, the leading edge, which interacts with the nozzle shear layer, provides a modest contribution at the blade tip, while the interaction with the inner shear layer is practically insignificant due to the lower rotational speed at the hub. This means that the main effect of inflow distortions on broadband noise is the change in RPM due to different mass-flow rates, which affects rotor self-noise.

Tonal noise predictions were carried out using a Green's function-based formulation in the frequency domain. Results show a very good agreement for loading noise and thus, in particular, for the case of uniform flow. For interaction tones, results are still considered to be good, as they are difficult to predict and a qualitative rise in sound pressure levels is captured. The directivity of the first blade passage frequency is also well captured by the model for the backward radiation, as good agreement is found in terms of both trends and levels. However, the physics involved in this discussion is complex and many phenomena have not yet been included in the mathematical model considered.

Declaration of competing interest

The authors declare that they have no known competing financial interests or personal relationships that could have appeared to influence the work reported in this paper.

Data availability

Data will be made available on request.

Acknowledgements

The authors would like to acknowledge the financial support of the Royal Academy of Engineering (RF\201819 \ 18 \ 194).

References

[1] FAA Aerospace Forecast. Federal Aviation Administration; 2019.
[2] MarketsandMarkets. Uav market by point of sale, systems, platform (civil & commercial, and defense & government), function, end use, application, type (fixed wing, rotary wing, hybrid), mode of operation, mtow range & region. global forecast to 2027 (September 2022).
[3] Schäffer B, Pieren R, Heutschi K, Wunderli JM, Becker S. Drone noise emission characteristics and noise effects on humans — a systematic review. Int J Environ Res Public Health 2021;18(11):5940. https://doi.org/10.3390/ijerph18115940.
[4] Morfey CL. Rotating blades and aerodynamic sound. J Sound Vib 1973;28(03):587–617. https://doi.org/10.1016/S0022-460X(73)80041-0.
[5] Hubbard H. Aeroacustics of flight vehicles: theory and practice. National Aeronautics and Space Administration; 1991.
[6] Marte JE, Kurtz DW. A review of aerodynamic noise from propellers, rotors, and lift fans. National Aeronautics and Space Administration; 1970.
[7] Williams JF, Hawkings D. Theory relating to the noise of rotating machinery. J Sound Vib 1969;10:10–21. https://doi.org/10.1016/0022-460X(69)90125-4.
[8] Xie J, Zhou Q, Joseph PF. Tone noise prediction of a propeller operating in nonuniform flows. AIAA J 2011;49(01). https://doi.org/10.2514/1.J050423.
[9] Meloni S, Proença AR, Lawrence JTL, Camussi R. An experimental investigation into model-scale installed jet–pylon–wing noise. J Fluid Mech 2021;929:A4. https://doi.org/10.1017/jfm.2021.831.
[10] Subramanian S, Mueller TJ. An experimental study of propeller noise due to cyclic flow distortion. J Sound Vib 1995;183(5):907–23. https://doi.org/10.1006/jsvi.1995.0295.
[11] Subramanian S. Experimental and computational studies on propeller noise due to inflow distortion. Ph.D. thesis. Indiana: Department of Aerospace and Mechanical Engineering Notre Dame; 1993.
[12] Roger M, Acevedo-Giraldo D, Jacob MC. Acoustic versus aerodynamic installation effects on a generic propeller-driven flying architecture. Int J Aeroacoust 2022;21(5–7):585–609. https://journals.sagepub.com/doi/abs/10.1177/1475472X221107372.
[13] Acevedo-Giraldo D, Roger M, Jacob MC. Experimental study of the aerodynamic noise of a pair of pusher-propellers installed over a wing. In: AIAA AVIATION 2023 forum; 2023.
[14] Paruchuri CC, Akiwate DC, Palleja-Cabre S, Karimian A, Joseph P, Parry A. Investigation into the mechanisms of propeller-wing interaction noise. https://doi.org/10.2514/6.2022-2936.
[15] Borchers IU, Scholten R, Gehlhar BW. Experimental results of the noise radiation of propellers in non-uniform flows. In: 10th AIAA aeroacoustics conference; 1986.
[16] Jamaluddin NS, Celik A, Baskaran K, Rezgui D, Azarpeyvand M. Experimental characterisation of small-scaled propeller-wing interaction noise. https://doi.org/10.2514/6.2022-2973.
[17] Di Marco A, Camussi R, De Paola E, Stoica LG, Paletta N, Aquilini C, et al. Experimental investigation of the aeroacoustic interaction effects of installed pusher propellers. https://doi.org/10.2514/6.2022-2833.
[18] Hanson DB. Spectrum of rotor noise caused by atmospheric turbulence. J Acoust Soc Am 1974;56(1):110–26. https://doi.org/10.1121/1.1903241.
[19] Majumdar SJ, Peake N. Noise generation by the interaction between ingested turbulence and a rotating fan. J Fluid Mech 1998;359:181–216. https://doi.org/10.1017/S0022112097008318.
[20] Gojon R, Doué N, Parisot-Dupuis H, Mellot B, Jardin T. Aeroacoustic radiation of a low Reynolds number two-bladed rotor in interaction with a cylindrical beam. https://doi.org/10.2514/6.2022-2972.
[21] Yauwenas Y, Fischer J, Moreau D, Doolan C. The effect of inflow disturbance on drone propeller noise. https://doi.org/10.2514/6.2019-2663, 2019.
[22] Wojno J, Mueller T, Blake W. Turbulence ingestion noise, Part 1: Experimental characterization of grid-generated turbulence. AIAA J 2002;40(1). https://doi.org/10.2514/2.1636.
[23] Wojno J, Mueller T, Blake W. Turbulence ingestion noise, Part 2: Rotor aeroacoustic response to grid-generated turbulence. Int J Environ Res Public Health 2002;40(1). https://doi.org/10.2514/2.1637.
[24] Jamaluddin NS, Celik A, Baskaran K, Rezgui D, Azarpeyvand M. Experimental analysis of a propeller noise in turbulent flow. Phys Fluids 2023;35(7):075106. https://doi.org/10.1063/5.0153326.
[25] Wang H, Zang B, Celik A, Rezgui D, Azerpeyvand M. An experimental investigation of propeller noise in forward flow. https://doi.org/10.2514/6.2019-2620, 2019.
[26] Storch V, Nozicka J, Brada M, Gemperle J, Suchy J. Measurement of noise and its correlation to performance and geometry of small aircraft propellers. https://doi.org/10.1051/epjconf/201611402112, 2016.
[27] Chaitanya P, Joseph P, Akiwate D, Parry AB, Prior SD. On the noise generation mechanisms of overlapping propellers. AIAA AVIATION Forum; 2021.
[28] Jung R, Kingan MJ, Dhopade P, Sharma RN. Investigation of the interaction tones produced by a contra-rotating unmanned aerial vehicle propeller. https://doi.org/10.2514/6.2022-2832.
[29] Gutin L. On the sound field of a rotating propeller. National Advisory Committee for Aeronautics; 1948.
[30] Kucukcoskun K. Prediction of free and scattered acoustic fields of low-speed fans. Ph.D. thesis. Von Karman Institute for Fluid Dynamics; 2012.
[31] Goldstein ME. Aeroacoustics. New York: McGraw–Hill; 1976.
[32] Lowson M, Ollerhead J. A theoretical study of helicopter rotor noise. J Sound Vib 1969;9(2):197–222. https://doi.org/10.1016/0022-460X(69)90028-5.
[33] Wright S. Sound radiation from a lifting rotor generated by asymmetric disk loading. J Sound Vib 1969;9(2):223–40. https://doi.org/10.1016/0022-460X(69)90029-7.
[34] Zhou Q, Joseph PF. Frequency-domain method for rotor self-noise prediction. AIAA J 2006;44(06). https://doi.org/10.2514/1.16176.
[35] Carley M. Sound from rotors in non-uniform flow. J Acoust Soc Am 2020. https://doi.org/10.1121/10.0001019.
[36] Glegg SAL, Kavashima E, Lachowski F, Devenport W, Alexander N. Inflow distortion noise in a non axisymmetric flow. In: 19th AIAA/CEAS aeroacoustics conference; 2013.
[37] Tontiwattanakul K. Signal processing for microphone arrays with novel geometrical design. Ph.D. thesis. UK: University of Southampton; 2016.
[38] Fanghzi Y. Characterization of propeller noise; 2021.
[39] Petricelli F, Palleja-Cabre S, Paruchuri CC, Joseph P, Karimian A, Meloni S, et al. On the effect of inflow distortions of propeller noise. https://doi.org/10.2514/6.2022-2938. https://arc.aiaa.org/doi/abs/10.2514/6.2022-2938.
[40] Theodorsen T. General theory of aerodynamic instability and the mechanism of flutter. May 1934. NACA TR No. 496.